Theor. Comput. Fluid Dyn. (2012) 26:311–318
DOI 10.1007/s00162-011-0234-x

ORIGINAL ARTICLE

Bahni Ray · P. Dinesh Sankar Reddy · Dipankar Bandyopadhyay · Sang Woo Joo · Ashutosh Sharma · Shizhi Qian · Gautam Biswas

Instabilities in free-surface electroosmotic flows

Received: 10 February 2011 / Accepted: 20 June 2011 / Published online: 10 July 2011

Abstract Instability of a thin electrolyte film undergoing a direct current electroosmotic flow has been investigated. The film with a compliant electrolyte–air interface is flowing over a rigid charged substrate. Unlike previous studies, inclusion of the Maxwell stresses in the formulation shows the presence of a new finite wavenumber shear-flow mode of instability, alongside the more frequently observed long-wave interfacial mode. The shear mode is found to be the dominant mode of instability when the electrolyte–solid and electrolyte–air interfaces are of opposite charge or of same charge but have very large zeta-potential at the electrolyte–air interface. The conditions for mode-switch (interfacial to shear) and the direction of the travelling waves are discussed through stability diagrams. Interestingly, the analysis shows that when the interfaces are of nearly same zeta potential, the 'free' electrolyte–air interface behaves more like a 'stationary' wall because of the ion transport in the reverse direction of the flow.

Keywords Electroosmotic flow · Linear stability analysis · Orr–Sommerfeld · Instability

1 Introduction

Recent technological advances in the miniaturised applications have attracted considerable interest in high-precision control over the flow of extremely small amount of liquids. Among the other electrokinetic methods to fuel up flows inside the small-scale devices [1–4], electroosmotic flow (EOF) is found to be one of the very

Communicated by Zikanov.

Electronic supplementary material The online version of this article (doi:10.1007/s00162-011-0234-x) contains supplementary material, which is available to authorized users.

B. Ray · G. Biswas
Department of Mechanical Engineering, Indian Institute of Technology, Kanpur 208016, UP, India

P. D. S. Reddy · A. Sharma (✉)
Department of Chemical Engineering, Indian Institute of Technology, Kanpur 208016, UP, India
E-mail: ashutos@iitk.ac.in

D. Bandyopadhyay
Department of Chemical Engineering, Indian Institute of Technology, Guwahati, 781039 Assam, India

S. W. Joo (✉) · A. Sharma · S. Qian
School of Mechanical Engineering, Yeungnam University, Gyongsan 712-749, South Korea
E-mail: swjoo@ynu.ac.kr

S. Qian
Department of Mechanical and Aerospace Engineering, Dominion University, Norfolk, VA 23529, USA

promising and versatile methods [5–9] because it allows facile flow control at less energy budget, is devoid of moving parts and is easier to fabricate in microfluidic circuits [10,11]. Since electroosmosis (EO) is governed by surface reactions, EOF is supposed to be more efficient in the micro or nano dimensions owing to the large surface-to-volume ratio. A number of reviews on the fundamentals of EOF can be found in the literature [1–4,12].

Among the other interesting aspects, the studies related to the interfacial deformations of thin films undergoing EOF are an exciting area of research because of the rich physics associated with it. Technologically, the interfacial instabilities of EOF can find many applications in the next generation microscale devices for mixing, cleaning, heat and mass transfer, and emulsification processes. The interfacial instabilities because of the EOF of a thin film are engendered by the coupled interaction between the applied electric field in the flow direction and the subsequent zeta potential gradient developed across the electrolyte film [13–27]. Recent studies [19–22] have reported the presence of an unconditional long-wave interfacial mode of instability for an open-channel EOF with free-boundary, employing widely accepted Gouy–Chapman–Stern model to formulate the electric field due to ion transport inside the electrolyte film. A number of studies have also shown the characteristics of the two-phase EOF inside microchannels assuming a non-deformable interface [10,11,13–17]. Interestingly, recent experimental studies [23,24] have shown that the instabilities at the free surface of a thin electrolyte film undergoing EOF exhibits reduction in speed because of the accumulation of surface charges. The electrical potential at the liquid-air free surface is generated by a preferential adsorption, accumulation, depletion or dissociation of ions near the surface compared with the bulk electrolyte. Even in a pure liquid, the preferred dipole orientations near the surface are responsible for surface potential [18]. Unlike all previous theoretical works [19–22], considering the Maxwell stresses in the governing equations and the boundary conditions [25–27], the wall-like behaviour of the free surface is explained by Choi et al. [28]. However, many issues such as the types of instability modes that prevail, the direction of the travelling waves under varied conditions, the parameter space for the wall-like behaviour of the electrolyte–air interface, etc. are very much among unexplored areas.

In this paper, considering the Maxwell stresses in the governing equations and the boundary conditions [25–27], we study the linearly unstable modes of the free surface of a thin electrolyte film employing an Orr–Sommerfeld (O–S) analysis (Fig. 1). Extending the study by Choi et al. [28], for the first time, we show the co-existence of both long-wave interfacial mode and finite-wavenumber shear-flow mode. The analysis also uncovers the travelling wave nature of the instabilities and predicts the direction of the waves. The study compares the dominant modes of instabilities for a range of key parameters, which can be of importance for future EOF applications.

2 Problem formulation

In this study, a two-dimensional EOF of an incompressible and Newtonian electrolyte is considered with density ρ, kinematic viscosity ν, dielectric coefficient ε, and mean thickness d. The EOF is driven by a direct

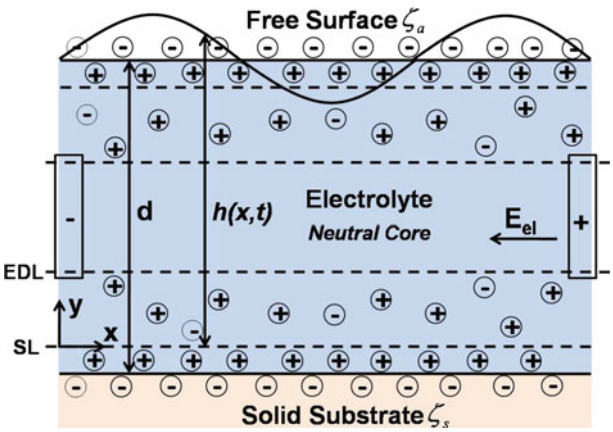

Fig. 1 Flow configuration for a two-dimensional electroosmotic flow (EOF) in a microchannel. *SL* Immobile shear layer, *EDL* Electric double layer (thickness of EDL exaggerated for clarity). The *sign* conventions in our formulation ensure EOF from *right to left*

current (DC) of electric field E_{el} in the direction of the flow, as shown in Fig. 1. The equations are formulated in a Cartesian coordinate system (x, y) with the origin fixed at the shear line (SL). The electrolyte flowing over a rigid charged surface develops zeta potentials ζ_s and ζ_a at the electrolyte–solid and electrolyte–air interfaces, respectively. The modelling of EOF involves the continuity and momentum equations from hydrodynamics and Maxwell's equations for the electrostatics [26,27]. Hydrodynamics and electrostatics are coupled through the interfacial stresses, leading to a set of coupled partial differential equations. The governing equations for such an EOF with Maxwell stress contributions can be expressed by the following non-dimensional forms:

$$\frac{D\mathbf{u}}{Dt} = -\nabla p + \nabla^2\mathbf{u} + \frac{E_O}{E_R}\nabla^2\phi\nabla\phi, \tag{2.1}$$

$$\nabla \cdot \mathbf{u} = 0. \tag{2.2}$$

Where, $\mathbf{u}\{u, v\}$, p, and ϕ are the velocity vector, pressure and the electric potential, respectively. The following dimensionless parameters are employed to obtain the above non-dimensional equations from their respective dimensional expressions, $\{x, h\} = \{x^*, h^*\}/d$; $t = t^*(\mu/\rho d^2)$; $\{u, v\} = \{u^*, v^*\}(\rho d/\mu)$; $p = p^*(\rho d^2/\mu^2)$; $\Gamma = \gamma(\rho d/\mu^2)$; $\phi = (\phi^*/E_{el}d)$; $E_O = (\varepsilon E_{el} d\zeta_s/\rho\nu^2)$; $E_R = (\zeta_s/E_{el}d)$; $E_{el} = (\phi_o/d_e)$. In these expressions, the notations with '$*$' represent dimensional variables and the notations γ, ϕ_o, and d_e represent the dimensional surface tension, the applied voltage and the distance between the electrodes, respectively. The dimensionless parameters E_O and E_R measure the electro-osmotic force and the zeta potential on the bottom surface, respectively. To complete the problem definition for the system shown in Fig. 1, no-slip and impermeability boundary conditions are imposed along the shear line (SL) as $\mathbf{u} = 0$ at $y = 0$, and the normal ($\mathbf{n}.\overline{\mathbf{T}}.\mathbf{n} = -\Gamma\kappa$) and tangential ($\mathbf{t}.\overline{\mathbf{T}}.\mathbf{n} = 0$) stress balance boundary conditions are enforced at the electrolyte–air interface ($y = h$). The notations $\mathbf{n}$, $\mathbf{t}$, κ and $\overline{\mathbf{T}}$ are the unit normal vector, unit tangent vector, curvature of the free surface, and total stress combining Maxwell and hydrodynamic stresses $[= \mu(\nabla\mathbf{u} + \nabla\mathbf{u}^T) + \varepsilon(\mathbf{EE} - 0.5(\mathbf{E}\cdot\mathbf{E})\mathbf{I})]$, respectively, where $\mathbf{E}$ is the electric field. The location of the free surface, $h(x, t)$ which is the local thickness of the electrolyte film is defined by the kinematic condition, $\dot{h} = -u(\partial h/\partial x) + v$.

The stresses from the electric field (ϕ) in Eq. 2.1 has contributions from the external field applied, ϕ_E, and from the zeta potentials, ϕ_ζ. In this study, the surface charge density is assumed to be fixed and no induced-charge is generated at the interface. To establish an axial field, a voltage, ϕ_o, is applied to one electrode while the other is earthed. This generates a reference dimensional field strength as $E_E = 1$. The field lines are perpendicular to the electrodes and parallel with the flow. In agreement with the Taylor–Melcher theory, the liquid is treated as an Ohmic conductor so the electric potential and electric field follow from solutions of Laplace's equation $\nabla^2\phi_E = 0$, with the field strength defined by $-\nabla\phi_E = E_E = 1$ [25–27]. The externally applied electric field (ϕ_E) is assumed to decay linearly across the electrodes, $(\partial\phi_E/\partial x) = -1$, which leads to the expression $\phi_E = -x$ after enforcing the boundary condition, $\phi_E = 0$ at $x = 0$. If we limit the present analysis to microchannels, where the dimensional Debye length λ_d is much smaller than d, the Poisson–Boltzmann equation with the Debye–Huckel approximation, $\nabla^2\phi_\zeta = (\phi_\zeta/De^2)$, reasonably expresses the potential distribution, where $De(= \lambda_d/d)$ is the Debye number. The electric field arising from the ζ-potentials is modelled by solving $\nabla^2\phi_\zeta = (\phi_\zeta/De^2)$, with the boundary conditions, $\phi_\zeta = E_R$, at $y = 0$ and $\phi_\zeta = E_R Z_R$, at $y = h$ where $Z_R = (\zeta_a/\zeta_s)$. The final expression obtained for the potential because of the difference in ζ-potentials at the interfaces is: $\phi_\zeta = E_R[\cosh(y/De) + A\sinh(y/De)]$. Combining the expressions for both the fields leads to the expression for the total potential,

$$\phi = -x + E_R[\cosh(y/De) + A\sinh(y/De)]. \tag{2.3}$$

Here, $A = [Z_R - \cosh(h/De)]/\sinh(h/De)$.

2.1 Base-state analysis

A unidirectional steady EOF with undisturbed free surface is obtained from the above system as $h = 1$, $v = 0$. The x-momentum equation in the base state, $\overline{u}(y) = E_O[\cosh(y/De) + \overline{A}\sinh(y/De)] + C_1 y + C_2$, along with the no-slip boundary condition, $\overline{u} = 0$ at $y = 0$ and the tangential stress balance, $\overline{u}_y = -(E_O/E_R)\overline{\phi}_{\zeta y}(\overline{\phi}_{\zeta x} - 1)$ at $y = 1$, leads to the following base-state profile,

$$\overline{u}(y) = E_O[\cosh(y/De) + \overline{A}\sinh(y/De) - 1], \tag{2.4}$$

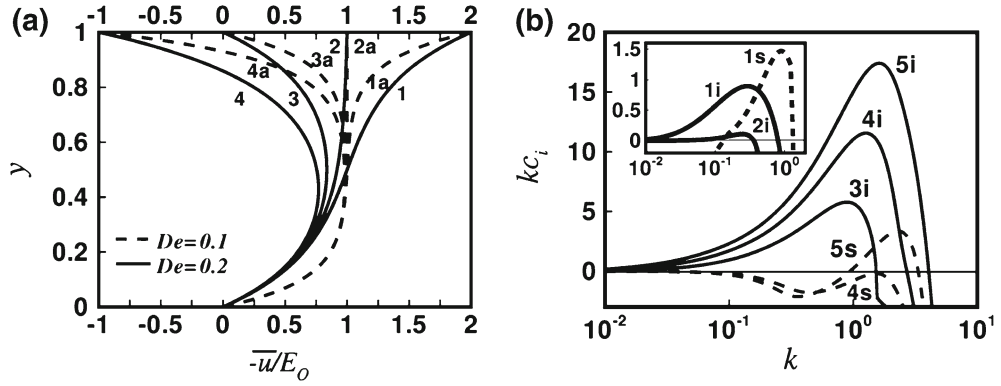

Fig. 2 Plot **a** shows the base-state velocity profiles, where *curves 1 (1a)–4(4a)* correspond to $Z_R = -1.0, 0, 1$ and 2, respectively. Plot **b** shows the variation of linear growth rate at different Z_R when $E_O = 9.0$. *Curves 1–5* correspond to $Z_R = -0.5, 0, 0.5, 1$ and 1.5, respectively, when $De = 0.2$. *Lines* labelled with '*i*' interfacial mode, those with '*s*' shear mode The other parameters used are $E_R = 1.0$ and $\Gamma = 100$

where $\overline{A} = [Z_R - \cosh(1/De)]/\sinh(1/De)$. The base-state velocity profile shows dependence on the free-surface zeta potential Z_R [26]. The fluid velocity on the free undeformed surface, $u(1) = -E_O(1 - Z_R)$ indicates that the electrolyte–air interface behaves like (i) a stationary wall at $Z_R = 1$, (ii) a shearing wall towards the EOF direction when $Z_R < 1$, generating additional flow, and (iii) a wall shearing in the reverse direction of the EOF when $Z_R > 1$, generating a reverse flow at the free surface. In Fig. 2a, the electrostatic response of the electrolyte–air interface for two different layer thicknesses is shown. It is important to note here that the sign conventions in our formulation ensure the direction of EOF from right to left. The thicker layer ($De = 0.1$) exhibits a plug-flow region near $y = 1/2$ with the velocity on the bottom and the free surface unaltered from that for the thinner layer ($De = 0.2$). When the free surface is electrically neutral ($Z_R = 0$), the plug flow continue till the surface, whereas when $Z_R > 0$ or $Z_R < 0$, the free surface reacts electrostatically to the electric field imposed like "a thread of volumeless but charged particles," and in turn imposes positive or negative shear stress to promote or hinder the EOF. A more detailed explanation about these base-state velocity profile is given elsewhere [28]. In essence, electric field generates EOF near a stationary solid surface, but generates an *electro-phoretic* flow for the charged free surface that can move like a charged suspension particle under the influence of applied electric field. The directions of these electro-osmotic and electro-phoretic flows are opposite for the same signs of the surface potentials on a fixed wall and on a mobile surface. Thus, a flow reversal can occur near the free surface for a large enough Z_R as electrophoresis of the charged free surface dominates in its vicinity. The experimental [23] and theoretical [29] evidences of similar velocity profiles are available in the literature.

2.2 Linear stability analysis

The stability of the unidirectional EOF can be studied by imposing small perturbations to the base-state profiles, $u = \overline{u} + u'$, $v = v'$, $\phi = \overline{\phi} + \phi'$, $p = \overline{p} + p'$ and $h = 1 + h'$, where the bars and primes on the variables denote mean and perturbed variables, respectively. The resulting perturbed governing equations and the boundary conditions are then linearised employing the normal modes, $u' = \delta[\tilde{u}(y)e^{ik(x-ct)}]$, $v' = \delta[\tilde{v}(y)e^{ik(x-ct)}]$, $p' = \delta[\tilde{p}(y)e^{ik(x-ct)}]$, $\phi' = \delta[\tilde{\phi}(y)e^{ik(x-ct)}]'$ and $h' = \delta[\tilde{h}(y)e^{ik(x-ct)}]$ where $\delta(<< 1)$, k and $c(= c_r + ic_i)$ are amplitude, wavenumber and phase speed of the infinitesimal perturbation, respectively, resulting in an eigenvalue problem analogous to the Orr–Sommerfeld (O–S) equation:

$$(D^2 - k^2)^2\tilde{v} = ik[(\overline{u} - c)(D^2 - k^2)\tilde{v} - \tilde{v}\overline{u}_{yy} + ((1/De^2) - k^2)(E_O/De^2)\overline{B}\tilde{h}\cosh(y/De)] + k^4(E_O E_R/De^2)\overline{B}[\sinh^2(1/De) + 0.5\overline{A}\sinh(2y/De)]\tilde{h}. \quad (2.5)$$

Here, D and subscript y denote d/dy and $\overline{B} = (Z_R\cosh(1/De) - 1)/\sinh^2(1/De)$. The boundary conditions on the rigid bottom ($y = 0$) are transformed to $\tilde{v} = \tilde{v}_y = 0$, whereas the free-surface ($y = 1$) boundary conditions are expressed as:

$$\left(\mathrm{d}^3\tilde{v}/\mathrm{d}y^3\right) - \left[\mathrm{i}k\left(\overline{u}-c\right)+3k^2\right]\left(\mathrm{d}\tilde{v}/\mathrm{d}y\right) + \mathrm{i}k\left[\tilde{v} - \overline{B}\left(E_\mathrm{O}/De^3\right)\sinh\left(1/De\right)\right]$$
$$- k^2\tilde{h}\left[2\mathrm{i}k\left(E_\mathrm{O}/De\right)\left(\overline{A}\cosh\left(1/De\right)+\sinh\left(1/De\right)\right) - 2\mathrm{i}k\left(\mathrm{d}\overline{u}/\mathrm{d}y\right) - \left(E_\mathrm{O}E_\mathrm{R}/De^3\right)\overline{BA} + k^2\Gamma\right] = 0,$$
$$\left(\mathrm{d}^2\tilde{v}/\mathrm{d}y^2\right) + k^2\tilde{v} + \left(E_\mathrm{O}E_\mathrm{R}/De^2\right)\left(k^2\overline{B}-1\right)\tilde{h}\sinh^2\left(1/De\right) + \left(E_\mathrm{O}E_\mathrm{R}/2De^2\right)\left(k^2\overline{B}-2\right)\overline{A}\tilde{h}\sinh\left(1/De\right)$$
$$- \mathrm{i}k\left(E_\mathrm{O}/De^2\right)\overline{B}\tilde{h}\cosh\left(1/De\right) + \left[\left(E_\mathrm{O}/E_\mathrm{R}\right) - \left(E_\mathrm{O}E_\mathrm{R}/De^2\right)\overline{A}^2\cosh^2\left(1/De\right)\right]\tilde{h} = 0,$$

$$\tilde{h} = \tilde{v}/\mathrm{i}k(\overline{u}-c). \tag{2.6}$$

The eigenvalue system is solved numerically using a spectral collocation method, which is easier to implement for nonlinear problems or problems with non-constant coefficient. The computational domain is mapped to $(-1, 1)$ for the liquid layer by employing the transformation $z = 2y - 1$, where $y = -1$ corresponds to the solid substrate and $y = 1$ correspond to the free interface. The resulting system is then solved by using the Chebyshev collocation algorithm with enhanced accuracy [30,31] to obtain the linear growth coefficient (kc_i) for a corresponding wavenumber (k) for instability.

3 Results and discussions

The typical magnitudes of dimensionless parameters (E_O, E_R, Γ) used in generating the following results are obtained based on the physically realistic ranges of the parameters [22]: $\rho \sim 1,000\,\mathrm{kg/m^3}$, $\mu \sim 0.001\mathrm{Pa\,s}$, $\varepsilon \sim 80$, $\varepsilon_0 = 8.85 \times 10^{-12}\,\mathrm{F/m}$, $d \sim 1$–$100\,\mu\mathrm{m}$, $\zeta_\mathrm{s}, \zeta_t \sim 10$–$100\,\mathrm{mV}$, $\phi_0 \sim 10$–$100\,\mathrm{V}$ and $\gamma \sim 0.05\,\mathrm{N/m}$. Figure 2b shows the variation in the linear growth rate kc_i with the wavenumber k for different values of the ratio of the zeta potentials at the electrolyte–air and electrolyte–solid interfaces, Z_R. The curves 1i and 1s indicate that when $E_\mathrm{O} = 9$ and $Z_\mathrm{R} < -0.3$, the strong applied field leads to a strong EOF and the additional inertia empowers the finite-wavenumber shear-flow instability to be the dominant mode. Interestingly, the condition $Z_\mathrm{R} < 0$ ensures that the interfaces are with opposing charge and the electrolyte–air interface behaves more like a 'shearing' wall moving towards the direction of the EOF as shown by the curve 1 of Fig. 2a. Thus, appearance of the dominant shear-flow mode can be attributed to the larger Reynolds stresses at the liquid layers because of the stronger flow rate engendered by the interface movement in the flow direction. In contrast, the curves 2 indicate when the core of the film displays more of plug-flow behaviour ($Z_\mathrm{R} = 0$), the more commonly found long-wave interfacial mode of instability [18,19,21] is the only existing mode. The figure also confirms that when the interface behaves like a 'stationary' wall ($Z_\mathrm{R} = 1$) or a 'shearing' wall with a velocity opposite to the flow direction ($Z_\mathrm{R} > 1$), the dominant long-wave interface mode (curves 4 and 5) coexists with the subdominant shear mode (broken curves 4s and 5s).

The finite wavenumber shear mode of instability in EOF can be more clearly understood in Fig. 3, where the maximum growth rate $(kc_i)_\mathrm{m}$, corresponding dominant wavenumber k_m, real phase speed c_rm corresponding to $(kc_i)_\mathrm{m}$ and critical wavenumber k_c are plotted against Z_R for two different film thicknesses, $De = 0.2$ (solid lines) and $De = 0.1$ (broken lines), at constant $E_\mathrm{R} = 1$ and $\Gamma = 100$. The k_m can be correlated to the dominant wavelength of instability,λ_m, by the relation $k_\mathrm{m} = 2\pi/\lambda_\mathrm{m}$. The critical wavenumber, k_c, is obtained by identifying the neutral stability condition, $kc_i = 0$. Similar to Fig. 2b, the curves in plot (a) of Fig. 3 shows that for $Z_\mathrm{R} < 0$, the shear mode [curves with label 's'] is the dominant mode of instability. Importantly, for a range of Z_R above zero, the long-wave interface mode [curves with label 'i'] is the dominant mode of instability before the shear mode become the dominant mode again at high Z_R. Under this situation the inertial force at the electrolyte–air interface is fuelled up by the motion of the interface in the opposite direction of the EOF. The value of Z_R at which the shift in the dominant mode occurs from interface to shear mode is comparatively low for a thicker film (curve 2s) than the same with a thinner film (curve 2s), which can be attributed to the larger inertial force because of the smaller viscous resistance at the electrolyte–air interface for a thicker film. The plots also reveal that as the zeta potential near the electrolyte–air interface diminishes ($Z_\mathrm{R} = 0$), the system is either more stable [minimum $(kc_i)_\mathrm{m}$] or completely stable [$(kc_i)_\mathrm{m} < 0$]. Plot (b) in this figure shows that the instability shows up a larger wavelength when $Z_\mathrm{R} = 0$ and progressively moves towards shorter wavelength under the conditions $Z_\mathrm{R} > 1$ or $Z_\mathrm{R} < 0$. Plots (a) and (b) together show that the films are more unstable due to lesser viscous resistance and evolve at a shorter wavelength when the film thicknesses are higher (lower De). It is important to note here that the EOF instabilities always travel across space as it grows because the eigenvalues (c) always contain a nonzero real part, c_r, along with the imaginary part c_i. Curves 1i and 2i in plot (c) show a clear change in direction of the travelling waves [change in sign of c_rm] when $\overline{u}$ at the interface changes its sign from positive to negative, with the variation in Z_R. The curves in

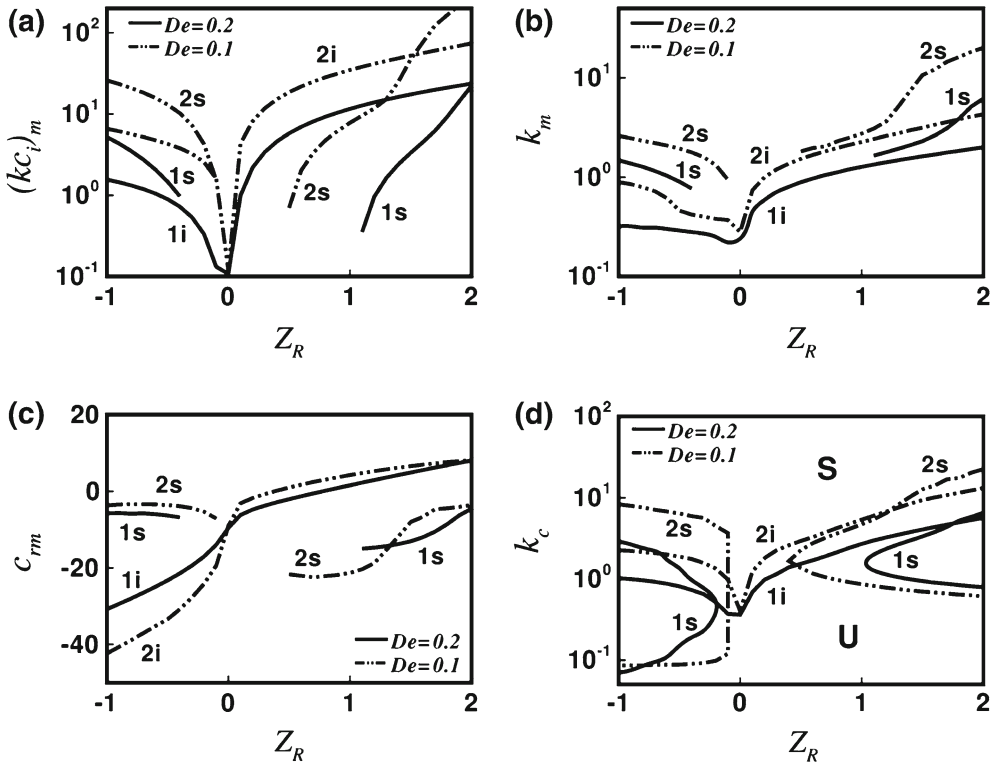

Fig. 3 Plots **a**–**d** show the variation of $(kc_i)_\mathrm{m}$, k_m, c_rm and neutral stability curves, respectively, with against Z_R at constant $E_\mathrm{O} = 9.0$ and for $De = 0.2$ (*solid lines*, *line* label 1) and $De = 0.1$ (*broken lines*, *line* label 2). *Lines* labelled with '*i*' interfacial mode, those with '*s*' shear mode and in plot **d**, *S* stable domain, *U* unstable domain. The other parameters used are $E_\mathrm{R} = 1.0$ and $\Gamma = 100$

plot (c) also supports the fact that the interface behave more like a (i) 'stationary' wall as c_rm tends to diminish near $Z_\mathrm{R} = 0$, (ii) 'shearing' wall in the direction of the flow when $Z_\mathrm{R} < 1$ and (iii) 'shearing' wall against the direction of the flow when $Z_\mathrm{R} > 1$. It is also very important to note here that change in the direction of the wave speed takes place only for the interface mode [curves 1i and 2i], whereas the shear-flow mode always travels [curves 1s and 2s] in the direction of the flow. The backward shearing motion of the interface only reduces the magnitude of the wave speed. The neutral stability diagrams in plot (d) more clearly depict the coexistence of both the interfacial and shear mode of instabilities. Curves 1i and 2i here correspond to interfacial mode of instability, which ensures the long-wave nature of the interfacial mode. The curves 1s and 2s depict the finite-wave number nature of the shear mode and demonstrate that this mode appears only after the EOF achieves a critical flow rate. For $Z_\mathrm{R} \approx 0$, the neutral stability diagram shows a single instability zone indicating the existence of solitary interfacial mode. However, for both $Z_\mathrm{R} \leq 0$ and $Z_\mathrm{R} > 0$ beyond a critical value of Z_R, the shear-flow mode coexist with the interfacial modes of instability [curves 1s and 2s]. The diagrams also show that the span of unstable wavenumber increases significantly as the film thickness is increased (lower De).

Figure 4 shows the influence of the external field strength (E_O) on the EOF. Plots (a) to (d) show the variations of $(kc_i)_\mathrm{m}$, k_m, c_rm and k_c with E_O at different Z_R. The curves 1 and 2 in plot (a) show that when $Z_\mathrm{R} \approx 0$, the interface mode is the only existing mode and progressively becomes more unstable as E_O is increased due to larger stresses from the electric field ($E_\mathrm{O} \propto E_\mathrm{el}$) at electrolyte–air interface. However, the curve 3 shows the coexistence of interface [3i] and shear-flow [3s] modes of instabilities at $Z_\mathrm{R} > 1$ and a dominant shear mode at high E_O where curve 3s crosses curve 3i. The figure confirms that the increase in electric field accelerates the flow, which leads to a dominant shear mode at very high E_O. The transition from the longer to shorter wavelength because of the switchover of the dominant mode from interface to shear-flow instability is also well supported by the plot (b). The c_rm curves in plot (c) show that the absolute wave speed of the travelling waves reduces as E_O is reduced and again we observe reverse flow for the interface mode when $Z_\mathrm{R} > 1$. Similar to plot 3(c), the shear mode always travel towards the EOF; however, the magnitude of

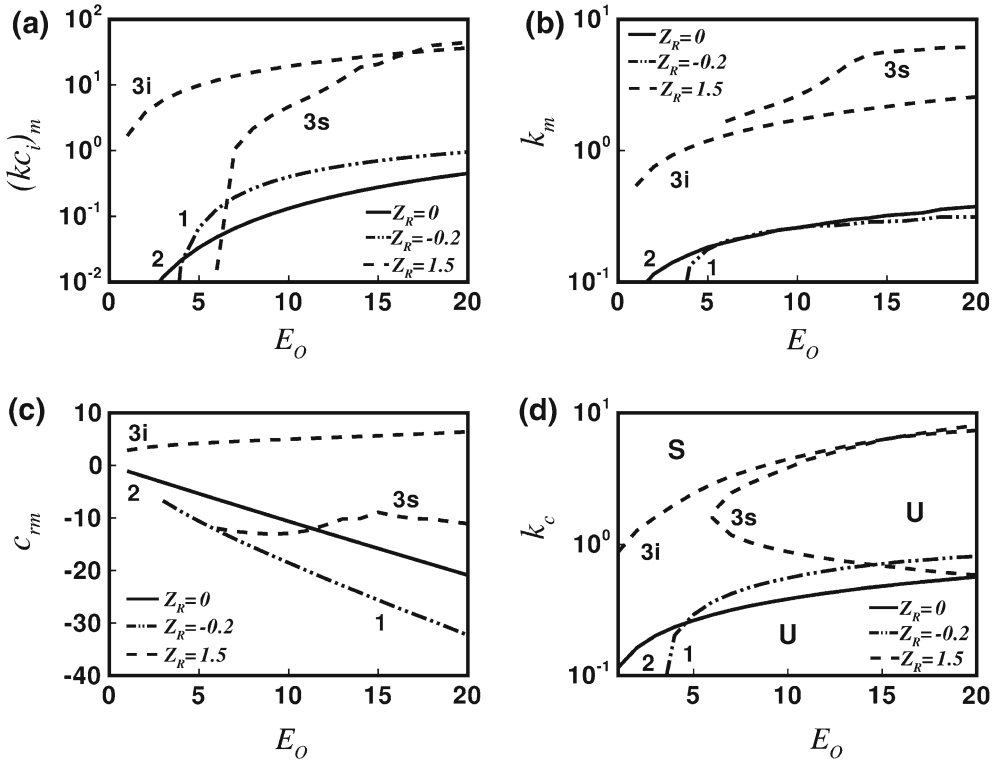

Fig. 4 Plots **a–d** show the variation of $(kc_i)_\mathrm{m}$, k_m, c_rm, and neutral stability curves, respectively with against E_O for $Z_\mathrm{R} = -0.2$, 0 and 1.5 (*curves* 1–3). *Lines* labelled with '*i*' interfacial mode, those with '*s*' shear mode and in plot **d**, *S* stable domain, *U* unstable domain. The other parameters taken are $E_\mathrm{R} = 1.0$, $De = 0.2$ and $\Gamma = 100$

wave speed of the travelling waves reduces as E_O reduces. The neutral stability diagrams in plot (d) indicate that the shear-flow instability originates beyond a critical value of E_O (=9 for $Z_\mathrm{R} = 1.0$ and =6 for $Z_\mathrm{R} = 1.5$).

4 Conclusions

We perform a linear stability of an electrolyte film with a compliant electrolyte–air interface and undergoing EOF on a charged rigid surface. Unlike most of the previous stability analyses [18–21] involving EOF, we consider the Maxwell stress contributions in the formulation. Along with the previously found long-wave interfacial mode of instability, a new finite wavenumber shear-flow mode, engendered by the strong applied field in the direction of the EOF, is uncovered for sufficiently higher flow rates. The interfacial mode originates because of the growth of surface waves under the strong influence of frictional forces present inside the film beyond a critical E_O and remains dominant when the free surface behaves more like a wall. Under the influence of an accelerating wall in or in the opposite direction of the flow increases the Reynolds stresses in the fluid layers, which develops the finite wavenumber shear mode. Further, in comparison with conventional pressure driven flows, for EOF, the additional stresses because of the movement of the charges/dipoles under the applied field add strength to the unstable modes. Interestingly, the analysis shows that it is the interfacial mode of instability which enforces the electrolyte–air interface to behave like a (A) 'stationary wall' when the zeta potential of the electrolyte–solid and electrolyte–air interfaces are similar, (B) 'shearing wall' towards the EOF direction when the interfaces are of opposing charge and (C) 'shearing wall' in the reverse direction of the EOF when the zeta potential of the electrolyte–air interface is very high. In contrast, the shear mode is always found to travel in the direction of the EOF with the variation in the magnitude of wave speed as the applied field strength is tuned. Another important observation is that for (thinner) films, lesser (larger) viscous resistance allows larger (lesser) inertial influence, which often leads to a dominant shear (interface) mode. Concisely, the study uncovers many interesting aspects of EOF instability of a thin electrolyte film, which can be of importance for many microfluidic, drug delivery, heat and mass transfer applications in future.

Acknowledgments This work was supported by World Class University Grant No. R32-2008-000-20082-0 of the Ministry of Education, Science and Technology of Korea.

References

1. Lyklema, J.: Fundamentals of Microfluidics. Academic Press, New York (1995)
2. Hunter, R.J.: Introduction to Modern Colloid Science. Oxford University Press, New York (1996)
3. Li, D.: Electrokinetics in Microfluidics. Eleseier, Amsterdam (2004)
4. Masliyah, J.H., Bhattacharjee, S.: Electrokinetic and Colloid Transport Phenomena. Wiley, New York (2006)
5. Anderson, J.L.: Colloid transport by interfacial forces. Ann. Rev. Fluid Mech. **21**, 61–99 (1989)
6. Yang, J., Lu, F., Kwok, D.Y.: Dynamic interfacial effect of electroosmotic slip flow with a moving capillary front in hydrophobic circular microchannels. J. Chem. Phys. **121**, 7443–7448 (2004)
7. Suresh, V., Homsy, G.M.: Stability of time-modulated electroosmotic flow. Phys. Fluids **16**, 2349–2356 (2004)
8. Hadermann, A.F., Waters, P.F., Woo, J.W.: High voltage electroosmosis. Pressure voltage behavior in the system—Alumina-2-Propanol. J. Phys. Chem. **78**, 65–69 (1974)
9. Iverson, B.D., Garimella, S.V.: Recent advances in microscale pumping technologies: a review and evaluation. Microfluid. Nanofluidics **5**, 145–174 (2008)
10. Brask, A., Goranovic, G., Bruus, H.: Electroosmotic pumping of nonconducting liquids by viscous drag from a secondary conducting liquid. Tech. Proc. Nanotech **1**, 190–193 (2003)
11. Brask, A., Goranovic, G., Jenson, M.J., Bruus, H.: A novel electro-osmotic pump design for nonconducting liquids: theoretical analysis of flow rate-pressure characteristics and stability. J. Micromech. Microeng. **15**, 883–891 (2005)
12. Stone, H.A., Stroock, A.D., Ajdari, A.: Engineering flows in small devices: microfluidics towards a lab-on-a-chip. J. Fluid Mech. **36**, 381–411 (2004)
13. Gao, Y., Wong, T.N., Yang, C., Ooi, K.T.: Transient two-liquid electroosmotic flow with electric charges at the interface. Colloid Surf. A **266**, 117–128 (2005)
14. Gao, Y., Wong, T.N., Yang, C., Ooi, K.T.: Two-fluid electroosmotic flow in microchannels. J. Colloid Interface Sci. **284**, 306–314 (2005)
15. Gao, Y., Wong, T.N., Chai, J.C., Yang, C., Ooi, K.T.: Numerical simulation of two fluid electroosmotic flow in microchannels. Int. J. Heat Mass Transf **48**, 5103–5111 (2005)
16. Gao, Y., Wang, C., Wong, T.N., Yang, C., Nguyen, N.T., Ooi, K.T.: Electro-osmotic control of the interface position of two-liquid flow through a microchannel. J. Micromech. Microeng. **17**, 358–366 (2007)
17. Ngoma, G.D., Erchiqui, F.: Pressure gradient and electroosmotic effects on two immiscible fluids in a microchannel between two parallel plates. J. Micromech. Microeng. **16**, 83–91 (2006)
18. McShea J., A., Callaghan, I.C.: Electrokinetic potentials at the gas-aqueous interface by spinning cylinder electrophoresis. Colloid Polym. Sci. **261**, 757–766 (1983)
19. Joo, S.W.: A new hydrodynamic instability in ultra-thin films induced by electroosmosis. J. Mech. Sci. Technol. **22**, 382–386 (2008)
20. Joo, S.W.: A nonlinear study on the interfacial instabilities in electroosmotic flows based on the Debye-Huckel approximation. Microfluid. Nanofluidics **5**, 417–423 (2008)
21. Qian, S., Joo, S.W., Jiang, Y., Cheney, M.A.: Free-surface problems in electrokinetic micro- and nanofluidics. Mech. Res. Commun. **36**, 82–91 (2009)
22. Sadiq, I.M.R., Joo, S.W.: Weakly nonlinear stability analysis of an electro-osmotic thin film free surface flow. Microgravity Sci. Technol. **21**, 331–343 (2009)
23. Lee, J.S.H, Li, D.: Electroosmotic flow at a liquid-air interface. Microfluid. Nanofluidics **2**, 361–365 (2006)
24. Lee, J.S.H., Barvulovic-Nad, I., Wu, Z., Xuan, X., Li, D.: Electrokinetic flow in a free surface-guided microchannel. J. Appl. Phys. **99**, 054905 (2006)
25. Melcher, J.R., Taylor, G.I.: Electrohydrodynamics: a review of the role of interfacial shear stresses. Annu. Rev. Fluid Mech. **1**, 111–146 (1969)
26. Saville, D.A.: Electrohydrodynamics: the Taylor–Melcher leaky dielectric model. Annu. Rev. Fluid Mech. **29**, 27–64 (1997)
27. Burcham, C.L., Saville, D.A.: Electrohydrodynamic stability: Taylor–Melcher theory for a liquid bridge suspended in a dielectric gas. J. Fluid. Mech. **452**, 163–187 (2002)
28. Choi, W.S., Sharma, A., Qian, S., Lim, G., Joo, S.W.: Is free surface free in micro-scale electrokinetic flows? J. Colloid Interface Sci. **347**, 153–155 (2010)
29. Wang, J., Wang, M., Li, Z.: Lattice Poisson–Boltzmann simulation of electro-osmotic flows in microchannels. J. Colloid Interface Sci. **296**, 729–736 (2006)
30. Weideman, J.A.C., Reddy, S.C.: A MATLAB differentiation matrix suite. ACM Trans. Math. Softw. **26**, 465–519 (2000)
31. Don, W.S., Solomonoff, A.: Accuracy and speed in computing the Chebyshev collocation derivative. SIAM J. Sci. Comput. **6**, 1253–1268 (1995)